Applied Catalysis B: Environmental 231 (2018) 43–50

Contents lists available at ScienceDirect

Applied Catalysis B: Environmental

journal homepage: www.elsevier.com/locate/apcatb

Amorphous nickel pyrophosphate modified graphitic carbon nitride: an efficient photocatalyst for hydrogen generation from water splitting

Ba-Ri Wulan[a,b], Sha-Sha Yi[b], Si-Jia Li[b], Yan-Xin Duan[b], Jun-Min Yan[a,b,*], Qing Jiang[b]

[a] State Key Laboratory of Automotive Simulation and Control, Jilin University, Changchun, 130022, China
[b] Key Laboratory of Automobile Materials (Jilin University), Ministry of Education, Department of Materials Science and Engineering, Jilin University, Changchun, 130022, China

ARTICLE INFO

Keywords:
$g\text{-}C_3N_4$
Amorphous
Nickel pyrophosphate
Photocatalyst
Hydrogen

ABSTRACT

A noble-metal-free amorphous $Ni_2P_2O_7$ modified $g\text{-}C_3N_4$ nanocomposite ($a\text{-}Ni_2P_2O_7/g\text{-}C_3N_4$) has been successfully prepared by a facile calcined process. The experimental results suggest that $a\text{-}Ni_2P_2O_7/g\text{-}C_3N_4$ displays the enhanced visible light absorption and improved charge separation relative to pristine $g\text{-}C_3N_4$, and shows smaller particle sizes and more negative conduction band edge potential than that of the crystalline $Ni_2P_2O_7$ modified $g\text{-}C_3N_4$ nanocomposite ($c\text{-}Ni_2P_2O_7/g\text{-}C_3N_4$), resulting in large amount of active sites and enhanced reduction capacity. The resultant $a\text{-}Ni_2P_2O_7/g\text{-}C_3N_4$ is evaluated as an excellent catalyst for photocatalytic hydrogen (H_2) generation under visible light irradiation, whose H_2 generation rate is almost 5 and 37 times higher than that of $c\text{-}Ni_2P_2O_7/g\text{-}C_3N_4$ and pristine $g\text{-}C_3N_4$, respectively, even better than that of $Pt/g\text{-}C_3N_4$. The improved activity of $a\text{-}Ni_2P_2O_7/g\text{-}C_3N_4$ is mainly ascribed to the good visible light utilization, efficient electron-hole pairs' separation and transfer, small particle sizes and high reduction ability of electron.

1. Introduction

The overusing of fossil fuels has made negative impact on the environment in the past years. Many efforts have been done to explore the environmental-benign energy to replace the traditional fuels. As a sustainable approach for new energy sources, photocatalytic hydrogen (H_2) generation utilizing solar energy from water splitting has attracted much attention [1,2]. Undoubtedly, the development of highly efficient and stable photocatalysts, especially on using earth-abundant semiconductors for H_2 generation from water splitting under visible light irradiation, is highly desired but remains a big challenge from the practical point of view [3,4].

Recently, graphitic carbon nitride ($g\text{-}C_3N_4$), which is composed of extremely abundant elements, has been regarded as one of the most promising photocatalysts for solar conversion, owning to its appealing chemical stability, environment friendliness, and capability of visible-light harvesting with band gap energy of 2.7 eV [5,6]. Unfortunately, $g\text{-}C_3N_4$ still faces a long way to meet the practical requirements on account of its fast recombination of photo-induced electrons and holes. Hence, in order to improve its photocatalytic efficiency, several methods have been employed, such as increasing surface area [7], protonation and polymerization [8], loading with co-catalysts [9], *etc*. Modifying noble metals, such as Pt [10], Ag [11] and Au [12], on $g\text{-}C_3N_4$ can efficiently improve the separation of electron-hole pairs. However, these noble metals are scarce and expensive, which is the serious barrier for their large scale application. Most recently, some very important non-noble metal-based materials, especially for Ni-based compounds, such as NiS [13], Ni_2P [14,15], $Ni(OH)_2$ [16], and NiO [17] have been reported as the excellent co-catalysts for photocatalytic H_2 generation. However, to the best of our knowledge, the use of non-precious Ni-based amorphous pyrophosphates for photocatalytic H_2 generation is rarely reported. Amorphous materials hold the high concentrations of unsaturated coordinative sites and the isotropic structures, and this usually makes the activities of its being superior to those of the crystalline ones [18,19]. On the other hand, development of synthesis method to obtain amorphous photocatalysts, not crystalline ones, is highly desired. Therefore, pursuit of high-effective, low-cost and non-noble amorphous co-catalysts to fabricate novel structure and further increase the activity of $g\text{-}C_3N_4$ to H_2 generation from water splitting is highly desirable and valuable.

Herein, as a proof-of-concept experiment, the amorphous nickel pyrophosphate ($a\text{-}Ni_2P_2O_7$) modified $g\text{-}C_3N_4$ ($a\text{-}Ni_2P_2O_7/g\text{-}C_3N_4$) has been successfully synthesized by calcining a mixture of $g\text{-}C_3N_4$ and $NiNH_4PO_4{\cdot}H_2O$ for the first time. Compared with the pristine $g\text{-}C_3N_4$, $a\text{-}Ni_2P_2O_7/g\text{-}C_3N_4$ displays the advanced visible light utilization and improved charge separation. Furthermore, the increased amount of

* Corresponding author.
E-mail address: junminyan@jlu.edu.cn (J.-M. Yan).

https://doi.org/10.1016/j.apcatb.2018.02.045
Received 25 November 2017; Received in revised form 16 January 2018; Accepted 20 February 2018
Available online 22 March 2018

active sites and robust reduction ability of electron can also be obtained relative to crystalline $Ni_2P_2O_7$ modified g-C_3N_4 (c-$Ni_2P_2O_7$/g-C_3N_4), which is contributed to the better photocatalytic activity for H_2 generation from water splitting under visible light irradiation, and is even superior to Pt/g-C_3N_4.

2. Experimental section

2.1. Chemicals

Urea (H_2NCONH_2, Sinopharm Chemical Reagent Co., Ltd., ≥99%), triethanolamine (TEOA, $(HOCH_2CH_2)_3N$, Sinopharm Chemical Reagent Co., Ltd., ≥78%), chloroplatinic acid hexahydrate ($H_2PtCl_6{\cdot}6H_2O$, Sinopharm Chemical Reagent Co., Ltd., ≥37% Pt basis), ammonia ($NH_3{\cdot}H_2O$, Beijing Chemical Works, 25.0–28.0%), ethylene glycol ($HOCH_2CH_2OH$, Sinopharm Chemical Reagent Co., Ltd., ≥99%), nickel nitrate hexahydrate ($Ni(NO_3)_2{\cdot}6H_2O$, Sinopharm Chemical Reagent Co., Ltd., ≥98.5%), sodium dihydrogen phosphate dehydrate ($NaH_2PO_4{\cdot}2H_2O$, Sinopharm Chemical Reagent Co., Ltd., ≥99%), sodium carbonate (Na_2CO_3, Beijing Chemicals Works, ≥99%), anhydrous ethanol (CH_3CH_2OH, Beijing Chemical works, ≥99.7%) and sodium sulfate anhydrous (Na_2SO_4, Beijing Chemicals Works, ≥99%). Nafion solution (5 wt.%, Dupont). Ultrapure water with the specific resistance of 18.2 MΩ·cm was obtained by reverse osmosis followed by ion-exchange and filtration.

2.2. Preparation of graphitic carbon nitride (g-C_3N_4)

The g-C_3N_4 was synthesized by directly heating urea in a muffle furnace at 600℃ for 4 h with a heating rate of 0.5 °C min^{-1}. The as-prepared yellow powder was obtained and then grinded.

2.3. Preparation of ammonium nickel phosphate ($NiNH_4PO_4{\cdot}H_2O$) precursor

The precursor was obtained by a one-step solvothermal process [20]. Typically, ethylene glycol (10 mL) was added into the concentrated $NH_3{\cdot}H_2O$ (10 mL) with stirring for 5 min to form an uniform mixture. Then, Na_2CO_3 (5 mL, 1 M), NaH_2PO_4 (7.5 mL, 1 M), and Ni $(NO_3)_2$ (5 mL, 1 M) were gradually added to the above liquid one by one at intervals of 5 min, and the final mixture was stirred for 1 h with the bright blue color. After that, the above mixed solution was transferred to a 50 mL Teflon-lined stainless-less autoclave, which was later maintained at 170 °C for 24 h. And then, the autoclave was cooled down to room temperature, and the precipitate was collected and washed with distilled water for three times and ethanol for once. The as-synthesized product was dried in vacuum at 60 °C overnight.

2.4. Preparation of amorphous (a-) and crystalline (c-) $Ni_2P_2O_7$

The a-$Ni_2P_2O_7$ was synthesized by calcining precursor of $NiNH_4PO_4{\cdot}H_2O$ in a muffle furnace at 500 °C for 2 h with a heating rate of 2 °C min^{-1}, and c-$Ni_2P_2O_7$ was obtained by the similar method but changing the calcining temperature to 600 °C.

2.5. Preparation of a-$Ni_2P_2O_7$/g-C_3N_4 and c-$Ni_2P_2O_7$/g-C_3N_4

Typically, the a-$Ni_2P_2O_7$/g-C_3N_4 was obtained as follows: firstly, $NiNH_4PO_4{\cdot}H_2O$ (48 mg) and g-C_3N_4 (400 mg) were ultrasonicated in ethanol (40 mL) for 30 min, and then magnetic stirred for 1 h. Secondly, the obtained mixture was washed by distilled water and dried at 60 °C for 10 h. After that, the as-prepared solid sample was grinded and put into an alumina crucible and calcined at 500 °C for 2 h with a heating rate of 2 °C min^{-1} to get the a-$Ni_2P_2O_7$/g-C_3N_4 with 12 wt.% of initial content of $NiNH_4PO_4{\cdot}H_2O$. The various loading contents of a-$Ni_2P_2O_7$ on g-C_3N_4 were also obtained by only changing the initial adding content of $NiNH_4PO_4{\cdot}H_2O$ (5, 8 and 15 wt.%). For comparison, the crystalline c-$Ni_2P_2O_7$/g-C_3N_4 (12 wt.%) was also synthesized by the similar method by altering the calcined temperature from 500 to 600 °C.

2.6. Characterizations

Wide angle X-ray diffraction (XRD) measurements were performed on a Rigaku D/max-2500pc X-ray diffractometer with Cu Kα irradiation (λ = 1.5406 Å) by a scan rate of 4° min^{-1}. Transmission electron microscope (TEM) analyses were performed using a JEOL JEM-2010 microscope (accelerating voltage = 200 kV). X-ray photoelectron spectroscopy (XPS) analyses were performed using an ESCALAB MK II (Vacuum Generators) spectrometer using Al Kα radiation (300 W). All binding energies were referenced to the C 1s peak at 284.6 eV of the surface adventitious carbon. Ultraviolet photoelectron spectroscopy (UPS) measurements were performed with an unfiltered He I (21.22 eV) gas discharge lamp at a total instrumental energy resolution of 100 meV. Ultraviolet-visible diffuse reflectance spectra (UV–vis DRS) were recorded on a Shimadzu UV-3600 spectrophotometer using the same amount of photocatalysts, in which $BaSO_4$ was used as the background. The photoluminescence (PL) spectra were detected on a Hitachi F-4500 fluorescence spectrophotometer with an excitation wavelength of 360 nm. Time-resolved photoluminescence (TRPL) spectra were recorded on a FLSP920 fluorescence lifetime spectrophotometer (Edinburgh, Instruments, UK) at an excitation wavelength of 360 nm. Fourier transform infrared spectroscopy (FTIR) of the samples were tested on a NEXUS-670 spectrometer at room temperature.

All electrochemical and photoelectrochemical tests were performed on a typical three-electrode system in 0.5 M Na_2SO_4 solution (PH = 6.8) on a CHI760E electrochemical workstation at room temperature using Ag/AgCl as the reference electrode, Pt mesh as the counter electrode, and catalyst films as the working electrodes. The photocurrent measurements were performed at an applied potential of 0 V versus Ag/AgCl (*vs.* Ag/AgCl) under visible light irradiation. A 300 W Xe lamp (CEL-HXF 300, 320 < λ < 2500 nm) equipped with a cut off filter (λ > 420 nm) was served as the light source. The electrochemical impedance spectroscopy (EIS) was determined over the frequency range from 0.01 to 100,000 Hz with an alternating current (AC) amplitude of 10 mV at the open circuit voltage in dark.

2.7. Photocatalytic activity for H_2 generation

Reactions were carried out in a Pyrex top-irradiation reaction vessel connected to a glass closed gas system. H_2 generation was achieved by dispersing 100 mg of photocatalyst (a-$Ni_2P_2O_7$/g-C_3N_4 with different initial adding contents of $NiNH_4PO_4{\cdot}H_2O$ (5, 8, 12 and 15 wt.%), c-$Ni_2P_2O_7$/g-C_3N_4 (12 wt.%) and pure g-C_3N_4) in aqueous solution (100 mL) containing 10 vol.% of TEOA as a sacrificial electron donor. The reaction system was degassed to remove air absolutely prior to irradiation under the Xe lamp (300 W) with a 420 nm cut off filter to remove the ultraviolet (UV) light. During the reaction, the temperature of the reaction solution was maintained at 8 °C by a flow of cooling water. The evolved gas was detected by gas chromatography (GC7900) equipped with a thermal conductive detector (TCD), using N_2 as the carrier gas.

2.8. Photocatalytic stability

The stability experiment was operated as below: the H_2 generation reaction was firstly tested for 3 h by using the method mentioned above. After that, all the H_2 generated in the gas system was removed completely. Then, the photocatalytic reaction was continued for another 3 h. As a result, the above reaction was performed three times (9 h in total).

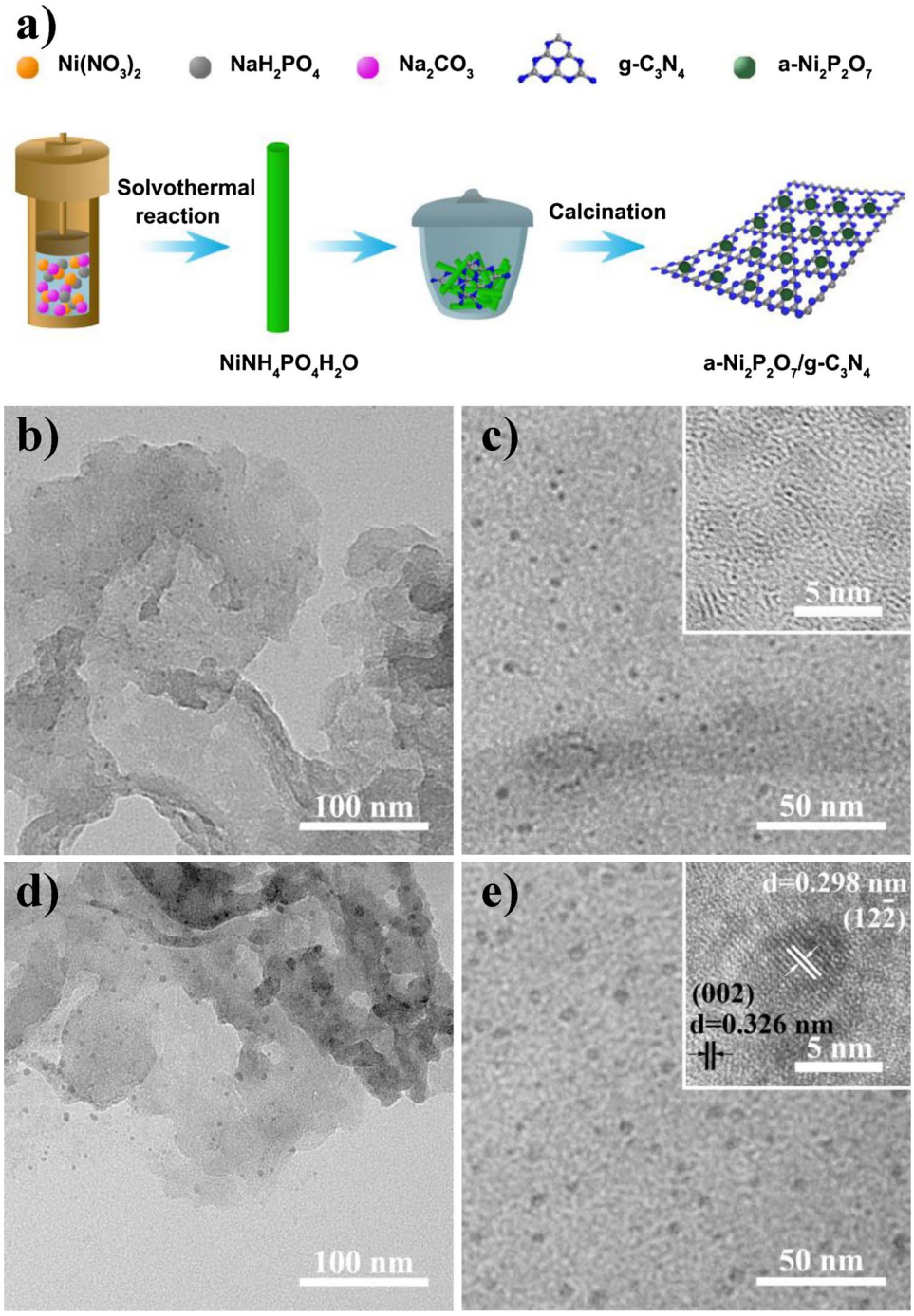

Fig. 1. (a) Scheme illustration of the preparation process for a-$Ni_2P_2O_7$/g-C_3N_4. (b,c) Low- and middle-magnification TEM images of a-$Ni_2P_2O_7$/g-C_3N_4 (Fig. 1c inset: HRTEM of a-$Ni_2P_2O_7$/g-C_3N_4). (d,e) Low- and middle-magnification TEM images of c-$Ni_2P_2O_7$/g-C_3N_4 (Fig. 1e inset: images of c-$Ni_2P_2O_7$ and g-C_3N_4). Initial weight percents of $NiNH_4PO_4{\cdot}H_2O$ in the specimens are both 12 wt.%.

3. Results and discussion

3.1. Structures and characterizations

The synthesis process for the a-$Ni_2P_2O_7$/g-C_3N_4 is illustrated in Fig. 1a. Typically, $NiNH_4PO_4{\cdot}H_2O$ nanorods (NRs) and g-C_3N_4 nanosheets (NSs) are prepared by solvothermal process and direct polycondensation of urea [20], respectively. And then, g-C_3N_4 is regarded as the substrate to be mixed with the as-prepared NRs and followed with the calcination at 500 °C in air. In this way, a-$Ni_2P_2O_7$ particles can be successfully obtained and loaded on the surface of the g-C_3N_4 NSs to form the a-$Ni_2P_2O_7$/g-C_3N_4 composite. Similarly, the c-$Ni_2P_2O_7$/g-C_3N_4 can also be synthesized only by altering the calcined temperature from 500 to 600 °C.

The morphology of the as-prepared specimens of a-$Ni_2P_2O_7$/g-C_3N_4 (12 wt.%) and c-$Ni_2P_2O_7$/g-C_3N_4 (12 wt.%) is characterized by the transmission electron microscope (TEM) and high resolution TEM (HRTEM). The a-$Ni_2P_2O_7$/g-C_3N_4 and c-$Ni_2P_2O_7$/g-C_3N_4 display the similar structure that the particles of $Ni_2P_2O_7$ are uniformly embedded on g-C_3N_4 NSs (Fig. 1b–e). It can be obviously observed from the middle resolution TEM images (Fig. 1c and e) that, the particle sizes of a-$Ni_2P_2O_7$ (1–4 nm, Fig. S1a) are slightly smaller than those of c-$Ni_2P_2O_7$ (4–9 nm, Fig. S1b), which may be due to the lower calcination temperature of a-$Ni_2P_2O_7$/g-C_3N_4 (500 °C) than that of c-$Ni_2P_2O_7$/g-C_3N_4

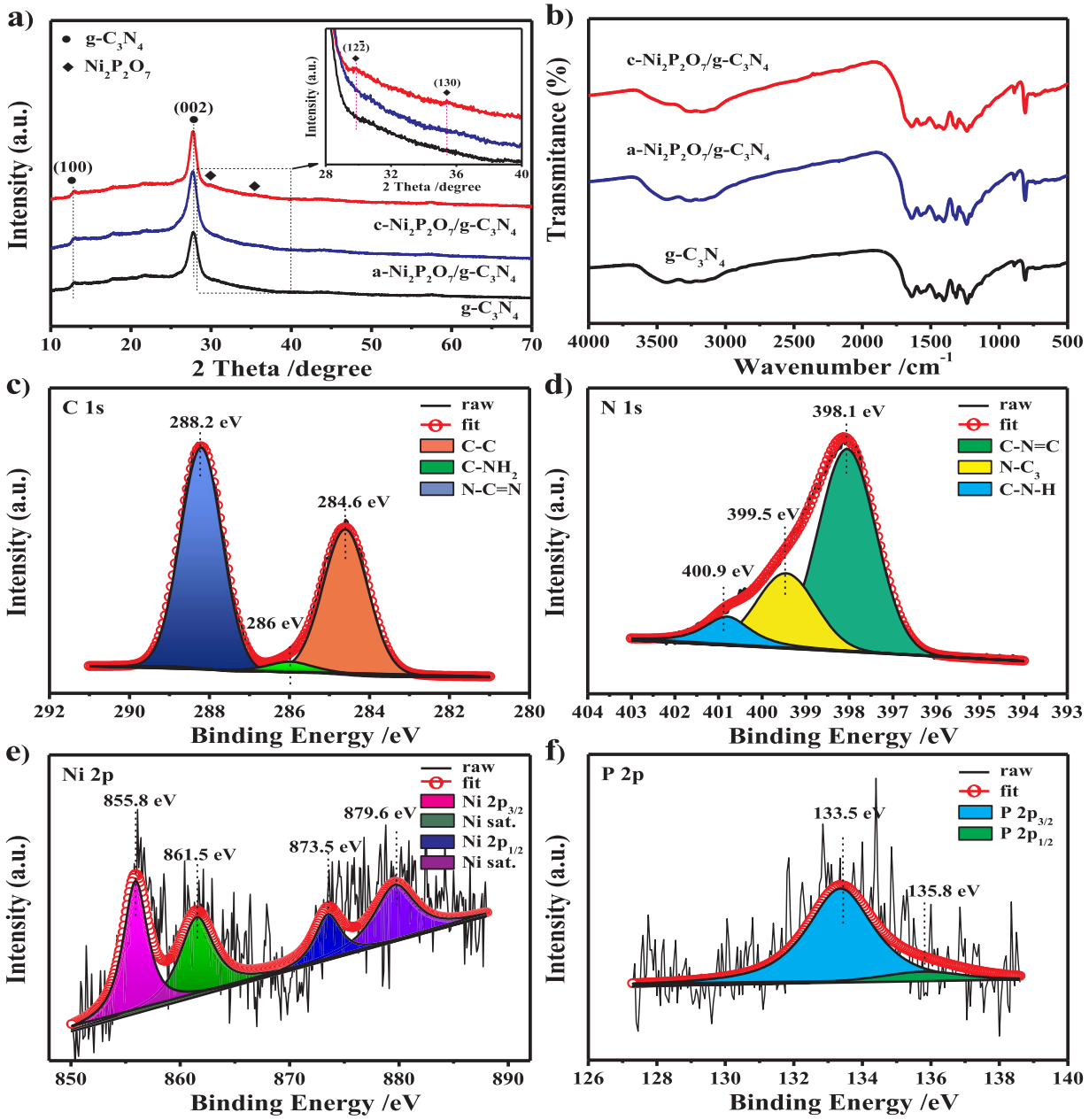

Fig. 2. (a) XRD patterns and (b) FTIR spectra of g-C_3N_4, a-$Ni_2P_2O_7$/g-C_3N_4 and c-$Ni_2P_2O_7$/g-C_3N_4. Inset of Fig. 2 (a): the enlarged view of the dotted area. XPS spectra of (c) C 1s, (d) N 1s, (e) Ni 2p and (f) P 2p in a-$Ni_2P_2O_7$/g-C_3N_4.

(600 °C) during the synthesis process. The HRTEM image of $Ni_2P_2O_7$/g-C_3N_4 (inset of Fig. 1e) clearly reveals lattice fringes spacing of 0.298 and 0.326 nm, corresponding to the (12$\bar{2}$) and (002) planes of $Ni_2P_2O_7$ and g-C_3N_4, respectively.

The structure and composition of the as-prepared samples are further investigated by the X-ray diffraction (XRD) patterns, Fourier transform infrared spectra (FTIR) and X-ray photoelectron spectroscopy (XPS). The XRD patterns of g-C_3N_4, a-$Ni_2P_2O_7$/g-C_3N_4 (12 wt.%) and c-$Ni_2P_2O_7$/g-C_3N_4 (12 wt.%) are showed in Fig. 2a, the structure of g-C_3N_4 can be obviously found in all the specimens. The strong peaks at 27.7° can be indexed as the (002) plane caused by the in-terlayer stacking of π-conjugated aromatic systems and the weak one at 13.3° is attributed to in-plane structural motif of g-C_3N_4 [21–23], respectively. No obvious peaks of $Ni_2P_2O_7$ can be found in a-$Ni_2P_2O_7$/g-C_3N_4, and this may be resulted from the amorphous state of $Ni_2P_2O_7$. For specimen of c-$Ni_2P_2O_7$/g-C_3N_4, except for two discernable peaks of g-C_3N_4, there are another two small characteristic diffraction peaks at 29.9 and 35.4° which can be indexed to phase of $Ni_2P_2O_7$ (JCPDS No. 39-0710) [24], indicating the formation of crystalline $Ni_2P_2O_7$. In Fig. 2b, the FTIR spectra of the three specimens have the similar peaks with no peak shift, where the peaks located at 3000–3500 cm^{-1} are attributed to the N—H stretching vibration and O—H vibration due to the uncondensed amino groups and physical adsorption of water [25], respectively. The wide absorption peaks in the range of 1100–1800 cm^{-1} are ascribed to the typical stretching modes of CN heteocycles [26]. In addition, the sharp peak at around 809 cm^{-1} is belonged to s-triazine ring modes of g-C_3N_4 [27]. Therefore, the presence of a- or c-$Ni_2P_2O_7$ has no influence in the structure of g-C_3N_4, which agrees well with the XRD results. In addition, the high resolution XPS spectra of a-$Ni_2P_2O_7$/g-C_3N_4 are also performed. Fig. 2c shows the XPS spectrum of C 1s are fitted with three peaks located at 284.6, 286.0 and 288.2 eV, respectively. The peak located at 284.6 eV can be attributed to the C—C bond from the XPS instrument itself, while the peak at 286.0 and 288.2 eV are assigned to C—NH_2 and N—C=N bonds of g-C_3N_4, respectively [28–30]. The N 1s in

Fig. 2d is separated into three peaks at binding energy values of 398.1, 399.5 and 400.9 eV, which are regarded as the N in bonds of C—N=C, N—$(C)_3$ and C—N—H, respectively [31]. As shown in Fig. 2e, the Ni 2p spectrum can be separated into two major peaks at 873.5 and 855.8 eV, corresponding to Ni $2p_{1/2}$ and Ni $2p_{3/2}$, respectively. The satellite peaks located at 879.6 and 861.5 eV are designed to the shake-up types of the Ni $2p_{1/2}$ and Ni $2p_{3/2}$, and all the peaks demonstrate the typical chemical states of Ni in $Ni_2P_2O_7$ [32]. The peaks centered at 135.8 and 133.5 eV prove the existence of P $2p_{1/2}$ and P $2p_{3/2}$, which are assigned as P in $Ni_2P_2O_7$ (Fig. 2f) [33].

In order to identify the composition of amorphous phase, the transformation process of $NiNH_4PO_4{\cdot}H_2O$ to $Ni_2P_2O_7$ is traced by XRD and FTIR analyses by changing calcination temperature of $NiNH_4PO_4{\cdot}H_2O$ from 25 to 600 °C. The XRD results (Fig. S2) show that, when temperature reaches 300 °C, the diffraction peaks of $NiNH_4PO_4{\cdot}H_2O$ (JCPDS No. 50-0425) [20] still can be observed even though the intensity is decreased obviously. However, the characteristic diffraction peaks of them are almost disappeared when temperature is up to 400 °C, which proves that the crystal structure of $NiNH_4PO_4{\cdot}H_2O$ is destroyed [34]. At 500 °C, there are no discernible peaks presented in the XRD pattern, indicating the formation of the amorphous phase. When the temperature reaches 600 °C, two obvious peaks can be observed, which are attributed to the phase of $Ni_2P_2O_7$ [24]. Therefore, it can be inferred that the amorphous phase obtained at 500 °C is composed of $Ni_2P_2O_7$. On the other hand, the FTIR spectra also prove the similar results (Fig. S3). At 300 °C, the FTIR peak intensity of $NiNH_4PO_4{\cdot}H_2O$ is gradually decreased due to the partial deamination and the dehydration of crystal water molecule [35]. With their further deamination, the band intensity of $NiNH_4PO_4{\cdot}H_2O$ is also reduced when the temperature reachs 400 °C. At 500 °C, a new weak band located at 530 cm^{-1} is assigned to the deformation of symmetrical P—O—P which is belonged to the internal modes of $P_2O_7^{4-}$, testifying the formation of the $Ni_2P_2O_7$ [36,37]. When the temperature is up to 600 °C, there is no apparent change between the samples which are calcined at 500 and 600 °C. It can be inferred that they have same functional groups corresponding to the $Ni_2P_2O_7$.

Ultraviolet-visible diffuse reflectance spectra (UV-vis DRS) and photoluminescence (PL) measurements are performed on a-$Ni_2P_2O_7$/g-C_3N_4, c-$Ni_2P_2O_7$/g-C_3N_4 and pure g-C_3N_4 for comparison. As shown in Fig. 3a, the pure g-C_3N_4 shows its fundamental absorption edge rising at 475 nm, which can be assigned to its intrinsic band gap of 2.60 eV (Fig. S4a) [38]. The absorption onset of a-$Ni_2P_2O_7$ and c-$Ni_2P_2O_7$ are about at 600 nm (Fig. S4b), which make it possible to sensitize g-C_3N_4 thus to increase the light response, corresponding to the band gaps of 2.24 and 2.13 eV (Fig. S4b, inset) [39], respectively. The a-$Ni_2P_2O_7$/g-C_3N_4 shows broader absorption in the visible light range relative to c-$Ni_2P_2O_7$/g-C_3N_4 and g-C_3N_4, demonstrating its highest capability for visible light harvesting. In Fig. 3b, the PL peak intensity of a-$Ni_2P_2O_7$/g-C_3N_4 is much lower than those of c-$Ni_2P_2O_7$/g-C_3N_4 and bare g-C_3N_4, which strongly indicates that addition of amorphous $Ni_2P_2O_7$ to g-C_3N_4 can efficiently accelerate the charge separation and transfer [40], and thus may lead to the enhanced photocatalytic H_2 generation performance (*vide infra*).

To further verify the improved charge separation and transfer efficiencies, the transient photocurrent-time (*i-t*) responses are also performed on a-$Ni_2P_2O_7$/g-C_3N_4, c-$Ni_2P_2O_7$/g-C_3N_4 and g-C_3N_4. As shown in Fig. 3c, no currents are detected for all the specimens when turns the light off, while currents are quickly increased once the light is turned on, indicating their good response to the visible light. Among the three specimens, a-$Ni_2P_2O_7$/g-C_3N_4 exhibits the strongest photocurrent intensity, indicating its most efficient photo-induced charge transfer and separation ability [41]. Furthermore, the separation efficiency and charge transfer resistance are also investigated by the electrochemical impedance spectroscopy (EIS) [33], as shown in Fig. 3d. The smaller radius implies the lower charge transfer resistance and faster transport rate of photo-induced charge carriers [42]. Consequently, the smallest radius of a-$Ni_2P_2O_7$/g-C_3N_4 proves its best efficiency on interfacial charge transfer relative to c-$Ni_2P_2O_7$/g-C_3N_4 and g-C_3N_4.

The time-resolved photoluminescence (TRPL) decay spectra are also performed. As shown in Fig. 4, the decay curves for pure g-C_3N_4, c-$Ni_2P_2O_7$/g-C_3N_4 and a-$Ni_2P_2O_7$/g-C_3N_4 are fitted and the corresponding $\tau_{av}$are calculated to be 2.23, 1.73 and 1.56 ns, respectively. The lifetime of a-$Ni_2P_2O_7$/g-C_3N_4 is much shorter than that of g-C_3N_4, indicating that effective charge transfer is achieved between g-C_3N_4 and a-$Ni_2P_2O_7$ [43]. Furthermore, the amorphous catalyst shows better charge transfer compared with the crystalline one, which reduces the recombination of photo-induced electrons and holes. Therefore, suggesting that more electrons are involved in H_2 generation.

3.2. Photocatalytic H_2 generation properties

Photocatalytic H_2 generation of the samples are evaluated under the visible light irradiation (Fig. 5a). After addition of $NiNH_4PO_4{\cdot}H_2O$ (5–15 wt.%) to form a-$Ni_2P_2O_7$, the composite specimens show much higher activities than that of pure g-C_3N_4. Especially, when the initial content of $NiNH_4PO_4{\cdot}H_2O$ reaches 12 wt.%, the obtained a-$Ni_2P_2O_7$/g-C_3N_4 shows the best H_2 generation rate of 207 μmol h^{-1} g^{-1}, which is about 37 times higher than that of pure g-C_3N_4 (5.5 μmol h^{-1} g^{-1}). Furthermore, the H_2 generation tests of a-$Ni_2P_2O_7$/g-C_3N_4 (12 wt.%), c-$Ni_2P_2O_7$/g-C_3N_4 (12 wt.%), Pt/g-C_3N_4 (0.5 wt.%) and g-C_3N_4 are also presented in Fig. 5b. It is obvious that a-$Ni_2P_2O_7$/g-C_3N_4 (207 μmol h^{-1} g^{-1}) exhibits much higher photocatalytic H_2 generation rate than that of c-$Ni_2P_2O_7$/g-C_3N_4 (41 μmol h^{-1} g^{-1}), and is even better than that of Pt/g-C_3N_4 (119 μmol h^{-1} g^{-1}). Namely, a-$Ni_2P_2O_7$ can act as a good co-catalyst to g-C_3N_4 when compared with c-$Ni_2P_2O_7$ and Pt. The apparent quantum efficency (QE) of H_2 generation over a-$Ni_2P_2O_7$/g-C_3N_4 at 420 nm is about 0.158% (Fig. 5c). Moreover, the as-prepared a-$Ni_2P_2O_7$/g-C_3N_4 (12 wt.%) also shows a good recycling stability, as shown in Fig. 5d, no obvious decline of H_2 generation rate can be detected after 3 recycling tests (total reaction time is 9 h). In addition, it can be found that the average rate of H_2 generation is slightly increased after the first recycling cycle, because the hydrogen generation reaction is an activated process, and the photons absorbed on the surface of the photocatalyst increase with increasing irradiation time [29,44].

3.3. Photocatalytic mechanism

To deeper explore the mechanism of enhanced photocatalytic H_2 generation performance, the positions of the lowest conduction band (E_{CB}) and the topmost valence band (E_{VB}) of g-C_3N_4, a-$Ni_2P_2O_7$ and c-$Ni_2P_2O_7$ are calculated with ultraviolet photoelectron spectroscopy (UPS) (Fig. S6). The ionization potential [equivalent to the valence band energy (E_{VB})] of g-C_3N_4, a-$Ni_2P_2O_7$ and c-$Ni_2P_2O_7$ can be calculated to be 1.59, 1.64 and 1.63 eV by subtracting the width of the He I UPS spectra from the excitation energy (21.22 eV). The E_{CB} for g-C_3N_4, a-$Ni_2P_2O_7$ and c-$Ni_2P_2O_7$ are estimated at −1.01, −0.60 and −0.50 eV from E_{VB}-E_g [45]. The E_{CB}, E_{VB} and E_g values of samples in electron volts (eV) are converted to electrochemical energy potentials in volts (V) based on the reference standard for which 0 V versus reversible hydrogen electrode (RHE) equals −4.44 eV versus E_{evac} (vacuum level) [46–48], which are summarized in Table S1.

On the basis of the above analysis, the possible mechanism for the improved photocatalytic H_2 generation activity of a-$Ni_2P_2O_7$/g-C_3N_4 can be speculated as follows (Scheme 1). The CB level of g-C_3N_4 is more negative than that of a-$Ni_2P_2O_7$, and the VB level of a-$Ni_2P_2O_7$ is also more positive than that of g-C_3N_4, forming a staggered band-gap type structure [49]. Consequently, CB-electrons in g-C_3N_4 can efficiently transfer to CB of a-$Ni_2P_2O_7$ under visible light irradiation, resulting in accumulation of electrons in CB of a-$Ni_2P_2O_7$ for reducing the H^+ to H_2. Meantime, the holes reserved in VB of a-$Ni_2P_2O_7$ can transfer to that of g-C_3N_4, oxidizing the TEOA to $TEOA^+$. In such a way, the separation of electron-hole pairs can be efficiently improved, decreasing the

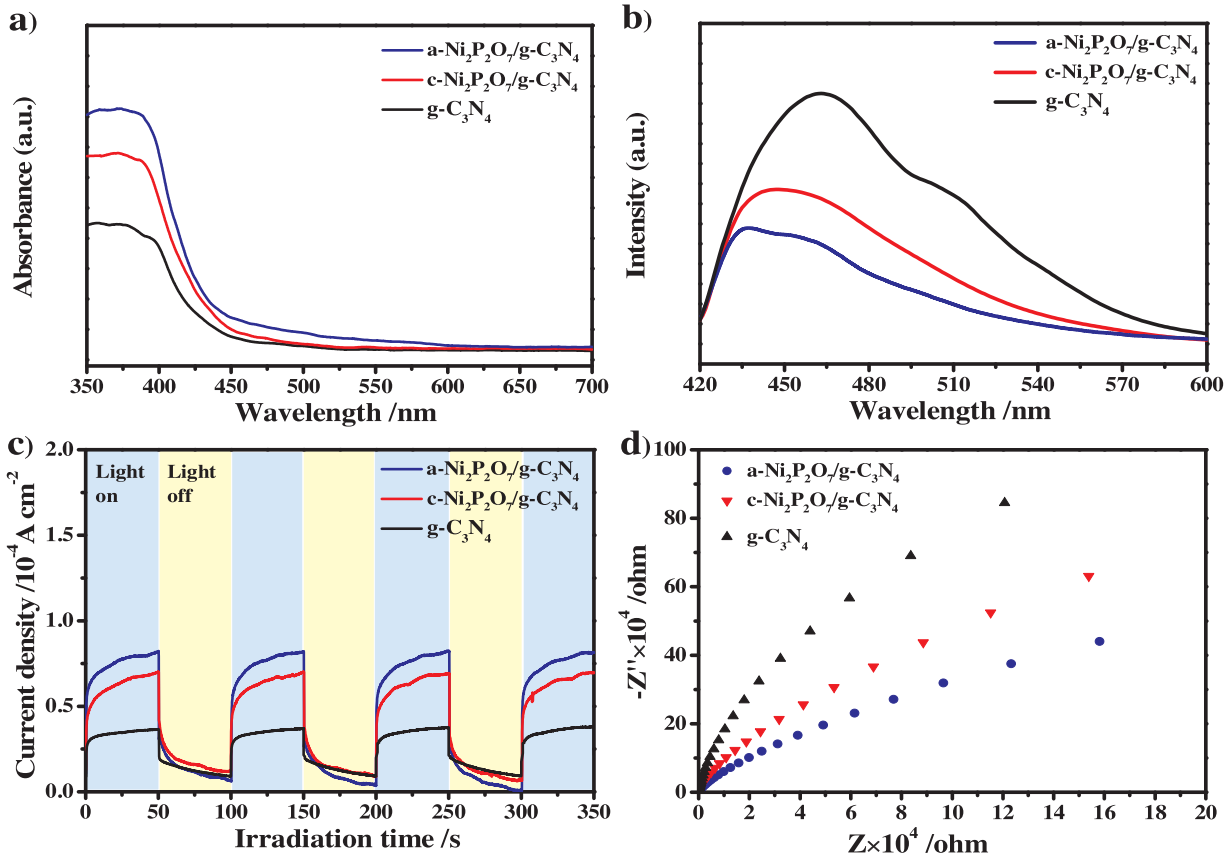

Fig. 3. (a) UV-vis DRS for g-C_3N_4, a-$Ni_2P_2O_7$/g-C_3N_4 and c-$Ni_2P_2O_7$/g-C_3N_4. (b) PL spectra of g-C_3N_4, a-$Ni_2P_2O_7$/g-C_3N_4 and c-$Ni_2P_2O_7$/g-C_3N_4 with an excitation wavelength of 360 nm. (c) Transient photocurrent responses of g-C_3N_4, a-$Ni_2P_2O_7$/g-C_3N_4 and c-$Ni_2P_2O_7$/g-C_3N_4 under visible light irradiation. (d) EIS plots of g-C_3N_4, a-$Ni_2P_2O_7$/g-C_3N_4 and c-$Ni_2P_2O_7$/g-C_3N_4 in dark.

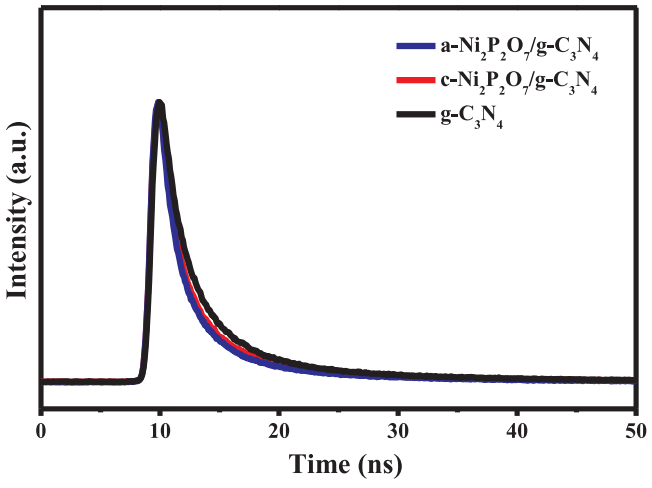

Fig. 4. TRPL decay spectra of g-C_3N_4, a-$Ni_2P_2O_7$/g-C_3N_4 and c-$Ni_2P_2O_7$/g-C_3N_4.

probability of photo-induced carrier recombination.

On the other hand, the reduction ability of its electrons has a relationship with CB edge position of the semiconductor in the conduction process. The more negative of the CB potential, the higher reduction ability of the electrons [50]. The CB level of a-$Ni_2P_2O_7$ has more negative potential relative to the crystalline one, leading to the more electrons participating to the reaction of H^+ reduction, which is consistent with the result of TRPL. Furthermore, with a-$Ni_2P_2O_7$ gradually transforms to the crystalline one, the increased particle sizes and the positively shifted CB potential bring to the negative effect on the photocatalytic H_2 generation [51]. Therefore, the advanced photocatalytic H_2 generation can be attributed to the efficient electron-hole pairs' separation and transfer, the strong reduction ability of CB-electron, the good visible light absorption ability as well as the small particle sizes.

4. Conclusions

In summary, the noble-metal-free amorphous $Ni_2P_2O_7$ modified g-C_3N_4 nanocomposite (a-$Ni_2P_2O_7$/g-C_3N_4) has been successfully synthesized by a facile calcination method. The amorphous state of a-$Ni_2P_2O_7$ on g-C_3N_4 exhibits the best photocatalytic performance compared with c-$Ni_2P_2O_7$/g-C_3N_4, g-C_3N_4 and even Pt/g-C_3N_4. The enhancement photocatalytic performance may be attributed to the good visible-light absorption ability, the efficient charge separation and transfer, high reduction capacity of CB-electron, and large amount of active sites. The present work may create a new insight for designing and synthesis of amorphous photocatalysts towards high efficiency and low-cost H_2 generation from water splitting by using solar energy.

Acknowledgements

This work is supported in part by the National Natural Science Foundation of China (51522101, 51631004, and 51471075); Program for JLU Science and Technology Innovative Research Team (2017TD-09); and the Fundamental Research Funds for the Central Universities.

Appendix A. Supplementary data

Supplementary material related to this article can be found, in the online version, at doi:https://doi.org/10.1016/j.apcatb.2018.02.045.

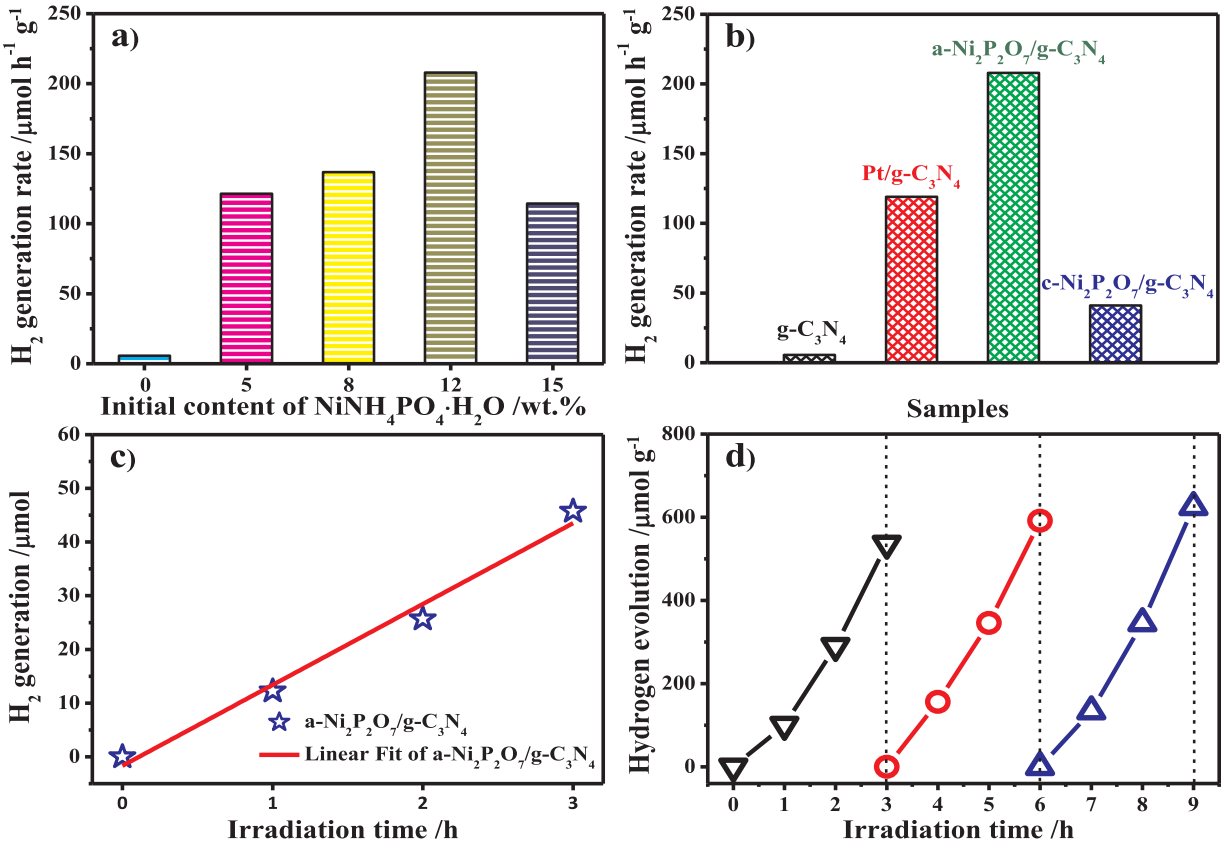

Fig. 5. (a) Comparison of the photocatalytic H_2 generation rates of a-$Ni_2P_2O_7$/g-C_3N_4 with different initial contents of $NiNH_4PO_4{\cdot}H_2O$ (0, 5, 8, 12 and 15 wt.%) under visible light irradiation (λ > 420 nm). (b) Photocatalytic H_2 generation activities on a-$Ni_2P_2O_7$/g-C_3N_4 (12 wt.%), c-$Ni_2P_2O_7$/g-C_3N_4 (12 wt.%), Pt/g-C_3N_4 (0.5 wt.% of Pt) and pure g-C_3N_4. (c) The apparent QE measurement of a-$Ni_2P_2O_7$/g-C_3N_4 at 420 nm in 10% TEOA aqueous solution. (d) Stability test of the photocatalytic H_2 generation of a-$Ni_2P_2O_7$/g-C_3N_4 (12 wt.%).

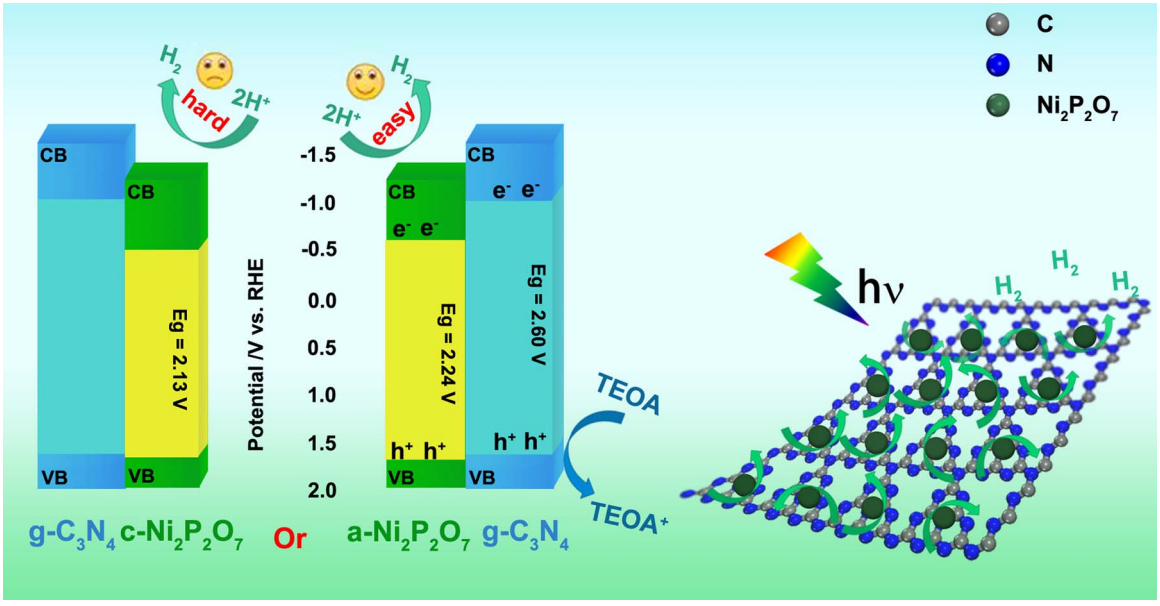

Scheme 1. Comparison of photocatalytic mechanism for a-$Ni_2P_2O_7$/g-C_3N_4 and c-$Ni_2P_2O_7$/g-C_3N_4.

References

[1] A. Fujishima, K. Honda, Nature 238 (1972) 37–38.
[2] X.Y. Liu, H. Chen, R. Wang, Y. Shang, Q. Zhang, W. Li, G. Zhang, J. Su, C.T. Dinh, F.P. de Arquer, J. Li, J. Jiang, Q. Mi, R. Si, X. Li, Y. Sun, Y.T. Long, H. Tian, E.H. Sargent, Z. Ning, Adv. Mater. 29 (2017) 1605646–1605653.
[3] Q. Lu, Y. Yu, Q. Ma, B. Chen, H. Zhang, Adv. Mater. 28 (2016) 1917–1933.
[4] Y. Shi, B. Zhang, Chem. Soc. Rev. 45 (2016) 1529–1541.
[5] A. Zada, M. Humayun, F. Raziq, X. Zhang, Y. Qu, L. Bai, C. Qin, L. Jing, H. Fu, Adv. Energy Mater. 6 (2016) 1601190–1601198.
[6] X. Chen, Q. Liu, Q. Wu, P. Du, J. Zhu, S. Dai, S. Yang, Adv. Funct. Mater. 26 (2016) 1719–1728.
[7] Y. Li, R. Jin, Y. Xing, J. Li, S. Song, X. Liu, M. Li, R. Jin, Adv. Energy Mater. 6 (2016) 1601273–1601277.
[8] D.J. Martin, P.J. Reardon, S.J. Moniz, J. Tang, J. Am. Chem. Soc. 136 (2014) 12568–12571.
[9] X. Yue, S. Yi, R. Wang, Z. Zhang, S. Qiu, Sci. Rep. 6 (2016) 22268–22276.

[10] X. Li, W. Bi, L. Zhang, S. Tao, W. Chu, Q. Zhang, Y. Luo, C. Wu, Y. Xie, Adv. Mater. 28 (2016) 2427–2431.
[11] M. Wu, J.M. Yan, X.W. Zhang, M. Zhao, Q. Jiang, J. Mater. Chem. A 3 (2015) 15710–15714.
[12] S. Samanta, S. Martha, K. Parida, ChemCatChem 6 (2014) 1453–1462.
[13] J. Wen, J. Xie, H. Zhang, A. Zhang, Y. Liu, X. Chen, X. Li, ACS Appl. Mater. Interfaces 9 (2017) 14031–14042.
[14] D.P. Kumar, J. Choi, S. Hong, D.A. Reddy, S. Lee, T.K. Kim, ACS Sustainable Chem. Eng. 4 (2016) 7158–7166.
[15] P. Ye, X. Liu, J. Iocozzia, Y. Yuan, L. Gu, G. Xu, Z. Lin, J. Mater. Chem. A 5 (2017) 8493–8498.
[16] J. Wang, Z. Wang, Z. Zhu, Appl. Catal. B: Environ. 204 (2017) 577–583.
[17] M.T. Uddin, Y. Nicolas, C. Olivier, W. Jaegermann, N. Rockstroh, H. Junge, T. Toupance, Phys. Chem. Chem. Phys. 19 (2017) 19279–19288.
[18] H. Yu, P. Xiao, P. Wang, J. Yu, Appl. Catal. B: Environ. 193 (2016) 217–225.
[19] X. Ge, L. Chen, L. Zhang, Y. Wen, A. Hirata, M. Chen, Adv. Mater. 26 (2014) 3100–3104.
[20] H. Zhang, Y. Feng, Y. Zhang, L. Fang, W. Li, Q. Liu, K. Wu, Y. Wang, ChemSusChem 7 (2014) 2000–2006.
[21] Q. Han, Z. Cheng, J. Gao, Y. Zhao, Z. Zhang, L. Dai, L. Qu, Adv. Funct. Mater. 27 (2017) 1606352–1606359.
[22] S. Zhang, N.T. Hang, Z. Zhang, H. Yue, W. Yang, Nanomaterials 7 (2017) 12–22.
[23] Z. Sun, C. Li, G. Yao, S. Zheng, Mater. Des. 94 (2016) 403–409.
[24] H. Zhang, Y. Lu, C.-D. Gu, X.-L. Wang, J.-P. Tu, CrystEngComm 14 (2012) 7942–7950.
[25] J. Qin, J. Huo, P. Zhang, J. Zeng, T. Wang, H. Zeng, Nanoscale 8 (2016) 2249–2259.
[26] H. Zhao, Y. Dong, P. Jiang, H. Miao, G. Wang, J. Zhang, J. Mater. Chem. A 3 (2015) 7375–7381.
[27] J. Liu, Y. Liu, N. Liu, Y. Han, X. Zhang, H. Huang, Y. Lifshitz, S.-T. Lee, J. Zhong, Z. Kang, Science 347 (2015) 970–974.
[28] B. Xue, H.Y. Jiang, T. Sun, F. Mao, Catal. Lett. 146 (2016) 2185–2192.
[29] S.S. Yi, J.M. Yan, B.R. Wulan, S.J. Li, K.H. Liu, Q. Jiang, Appl. Catal. B: Environ. 200 (2017) 477–483.
[30] D. Gao, Q. Xu, J. Zhang, Z. Yang, M. Si, Z. Yan, D. Xue, Nanoscale 6 (2014) 2577–2581.
[31] N. Tian, H. Huang, Y. He, Y. Guo, Y. Zhang, Colloids Surf. A: Physicochem. Eng. Asp. 467 (2015) 188–194.
[32] C. Wei, C. Cheng, S. Wang, Y. Xu, J. Wang, H. Pang, Chem. Asian J. 10 (2015) 1731–1737.
[33] B. Senthilkumar, Z. Khan, S. Park, K. Kim, H. Ko, Y. Kim, J. Mater. Chem. A 3 (2015) 21553–21561.
[34] W. Wu, S. Li, X. Wu, S. Liao, J. Cao, Chin. J. Chem. 28 (2010) 2389–2393.
[35] G. Berhault, P. Afanasiev, H. Loboue, C. Geantet, Inorg. Chem. 48 (2009) 2985–2992.
[36] U.C. Chung, J.L. Mesa, J.L. Pizarro, I. de Meatza, M. Bengoechea, J. Rodríguez Fernández, M.I. Arriortua, T. Rojo, Chem. Mater. 23 (2011) 4317–4330.
[37] A. Ben Rhaiem, S. Chouaib, K. Guidara, Ionics 16 (2010) 455–463.
[38] J. Ma, C. Wang, H. He, Appl. Catal. B: Environ. 184 (2016) 28–34.
[39] J. Fu, B. Chang, Y. Tian, F. Xi, X. Dong, J. Mater. Chem. A 1 (2013) 3083–3090.
[40] H. Yu, R. Shi, Y. Zhao, T. Bian, Y. Zhao, C. Zhou, G.I. Waterhouse, L.Z. Wu, C.H. Tung, T. Zhang, Adv. Mater. 29 (2017) 1605148–1605154.
[41] J. Zhang, L. Qi, J. Ran, J. Yu, S. Qiao, Adv. Energy Mater. 4 (2014) 1301925–1301930.
[42] X. Yu, R. Du, B. Li, Y. Zhang, H. Liu, J. Qu, X. An, Appl. Catal. B: Environ. 182 (2016) 504–512.
[43] Z. Sun, H. Zheng, J. Li, P. Du, Energy Environ. Sci. 8 (2015) 2668–2676.
[44] J. Zhang, Y. Wang, J. Jin, J. Zhang, Z. Lin, F. Huang, J. Yu, ACS Appl. Mater. Interfaces 5 (2013) 10317–10324.
[45] L.J. Zhang, S. Li, B.K. Liu, D.J. Wang, T.F. Xie, ACS Catal. 4 (2014) 3724–3729.
[46] Y. Shi, J. Chen, Z. Mao, B.D. Fahlman, D. Wang, J. Catal. 356 (2017) 22–31.
[47] J. Liu, Y. Yang, N. Liu, Y. Liu, H. Huang, Z. Kang, Green Chem. 16 (2014) 4559–4565.
[48] J. Liu, N.Y. Liu, H. Li, L.P. Wang, X.Q. Wu, H. Huang, Y. Liu, F. Bao, Y. Lifshitz, S.T. Lee, Z.H. Kang, Nanoscale 8 (2016) 11956–11961.
[49] H. Wang, L. Zhang, Z. Chen, J. Hu, S. Li, Z. Wang, J. Liu, X. Wang, Chem. Soc. Rev. 43 (2014) 5234–5244.
[50] W. Luo, Z. Li, X. Jiang, T. Yu, L. Liu, X. Chen, J. Ye, Z. Zou, Phys. Chem. Chem. Phys. 10 (2008) 6717–6723.
[51] I. Grigioni, M. Bernareggi, G. Sinibaldi, M.V. Dozzi, E. Selli, Appl. Catal. A: Gen. 518 (2016) 176–180.